Monte Carlo study of crystalline order and defects on weakly curved surfaces

A. Hexemer*
Materials Department, UC Santa Barbara, Santa Barbara, California 93106-5050, USA

V. Vitelli
Department of Physics and Astronomy, 209 South 33rd Street, University of Pennsylvania, Philadelphia, Pennsylvania 19104-6396, USA

E. J. Kramer†
Materials Department, UC Santa Barbara, Santa Barbara, California 93106-5050, USA and Department of Chemical Engineering, UC Santa Barbara, Santa Barbara, California 93106-5080, USA

G. H. Fredrickson
Department of Chemical Engineering, UC Santa Barbara, Santa Barbara, California 93106-5080, USA
(Received 26 March 2007; revised manuscript received 2 September 2007; published 29 November 2007)

We numerically study the ground states of particles interacting via a repulsive Yukawa potential on two rigid substrates shaped as isolated and periodically arranged bumps characterized by a spatially varying Gaussian curvature. Below a critical aspect ratio that describes the substrate deformation, the lattice is frustrated, but defect free. A further increase of the aspect ratio triggers defect unbinding transitions that lower the total potential energy by introducing dislocations either in isolation or within grain boundaries. In the presence of very strong deformations, isolated disclinations are nucleated. We show that the character and spatial distribution of defects observed in the ground state reflect the symmetries and periodicity of the two model surfaces investigated in this study.

DOI: 10.1103/PhysRevE.76.051604 PACS number(s): 68.15.+e, 61.50.Ah, 61.72.Bb

I. INTRODUCTION

The study of crystalline arrays of particles on curved surfaces has a rich history starting approximately over 100 years ago with the well-known Thomson problem [1]. The original problem of determining the ground state of classical electrons confined on a sphere has fueled a broader interest in the influence of geometric constraints on particle packings. A variety of experimental realizations have been discovered including viral architecture [2], flower pollen like the Morning Glory, cytoplasmic acidification on a clathrin lattice morphology [3,4], colloidal encapsulation for drug delivery [5,6], and multielectron bubbles on the surface of liquid helium [7]. Other experimentally ordered structures on nonuniform curved surfaces including lipid bilayers [8], Langmuir films, wrinkled surfaces [9], and liquid crystal thin films are of great scientific interest.

The properties of two-dimensional crystals constrained on surfaces of constant curvature have been the object of extensive theoretical studies. The main focus remains, however, on spherical geometry with the advantage of experimental interest and uniform, well-defined positive curvature [10–15], but also more abstract surfaces of constant negative curvature have been analyzed often in connection with models of glasses [16]. The study of the ground state of large numbers of particles on a sphere has proven to be very challenging and is still under investigation. The major complication, from an analytical as well as from a simulation standpoint, is the vast configurational space riddled with local minima having very small differences in energy. A crucial simplification follows from the fact that the integrated Gaussian curvature $K(r)$ of the substrate constrains the net topological charge of the defects according to the following relation [17,18]:

$$\sum_z (6-z)N_z = \frac{3}{\pi}\int\int_s \sqrt{g}\, d^2r\, K(r), \tag{1}$$

where N_z is the number of particles with coordination z in the region s and g is the determinant of the metric tensor of the surface. A sphere has a constant Gaussian curvature $K=\frac{1}{R^2}$, where R is the radius of the sphere, and the right-hand side of Eq. (1) can be evaluated to yield 12. A sphere, covered with a hexagonal lattice containing more than 12 particles, will exhibit 12 more fivefold than sevenfold disclinations due to the integrated Gaussian curvature of the confining manifold. In the ground state, the fivefold defects are sitting at the vertices of a regular icosahedron. In flat space, disclinations are expensive energetically; their energy grows with the size of the system squared ($E_{disclination} \propto R^2$, where R is the characteristic size of the system). The main contribution to the energy comes from the elastic stretching of the lattice, in addition to a core energy of the disclination. Isolated disclinations are, therefore, never observed for larger systems in the ground state of a flat surface in contrast to curved space, where disclinations may be forced in by topological requirements. Furthermore, if the ratio $\frac{R}{\alpha}$ of the sphere radius to lattice constant α is increased above a critical value, the ground state contains grain boundaries attached to the 12

*Currently at Lawrence Berkeley National Lab, 1 Cyclotron Road, Berkeley, CA 94720.
†edkramer@mrl.ucsb.edu

disclinations to screen the lattice strain [13,14,16]. The critical ratio is a balance between the decrease in strain energy of the lattice caused by incorporating the grain boundaries and the energy required to create them.

Less work has been done on surfaces of varying Gaussian curvature [19,20]. A simple illustration is provided by deforming a plane into a bump so that positive Gaussian curvature is generated near the top of the hill and negative Gaussian curvature in the outskirts at radial distances greater than its inflection point. Such a curved substrate could be engineered by using a template of melted colloidal particles later coated with a hexagonal array of spheres generated by the self-assembly of block copolymers [21].

Since the integrated Gaussian curvature of such a bumpy landscape is zero, an equal number of fivefold and sevenfold disclinations is expected from Eq. (1). The interesting aspect is the long-range interaction between the defects and the varying curvature of the substrate that acts as a source for the topological charges in analogy with the more familiar case of electrostatic particles in a smeared out charge distribution [10,19,22,23]. This geometric potential extends well beyond the range of the interparticle interaction because it is controlled by the length scale over which the Gaussian curvature varies and it is naturally absent in flat space. Recent theoretical work has explored various aspects of frustrated hexagonal lattices confined on a model surface shaped as an isolated Gaussian bump [19]. For small deformations (i.e., below a critical aspect ratio of the bump height a over variance σ), a hexagonal lattice of particles wraps defect free over the deformed substrate. The curvature is accommodated by inducing a nonuniform strain in the lattice.

The creation of defects, screening the Gaussian curvature, is governed by the frustration in the lattice and the energy penalty for creating a defect. A frustrated lattice is characterized by the fact that the individual interparticle distance differs from its *relaxed* constant value in the flat-space ground state. Upon increasing the aspect ratio above a critical value ξ_c (controlled mainly by the underlying geometry), a new ground state emerges characterized by two dislocations placed at a radial distance of approximately 1.1σ on opposite sides of the Gaussian bump so that the total Burgers vector is equal to zero. (In Fig. 1, the common defects in hexagonal lattices are shown along with the Burgers vector for the dislocations [24].) The exact equilibrium separation of the defect pair was calculated by finding the minimum of the geometric potential between each dislocation and the curvature with a small correction arising from the interaction between the two dislocations. These analytical results were corroborated by numerical calculations using a fixed connectivity model [19].

The purpose of this study is to numerically investigate via Monte Carlo simulations the distribution of two or more defects in the ground state of crystalline monolayers confined on surfaces of varying Gaussian curvature and compare the results retrieved to the calculations of Ref. [19]. The method we present can be easily employed to determine the defected ground states of complex surface deformations, with no azimuthal symmetry without the artificial restrictions inherent in the previous fixed connectivity minimizations in which the local coordination was constrained to be sixfold by construction except at the locations of isolated defects [19]. We first test the theoretical predictions for an isolated Gaussian bump and later proceed to study numerically a rigid substrate described by perpendicular intersecting sine waves. Novel defect morphologies are generated from breaking the azimuthal symmetry of an isolated bump.

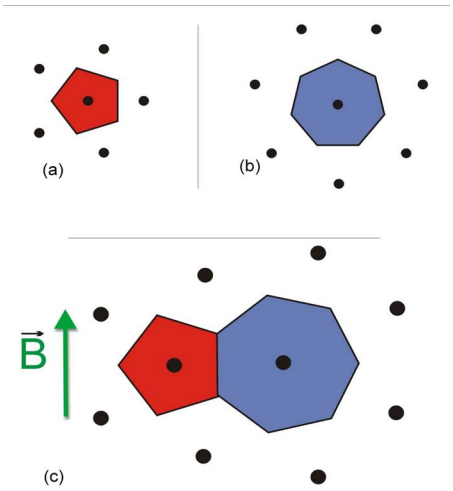

FIG. 1. (Color online) (a) Fivefold disclination, in red, showing the Voronoi cell with five nearest neighbors. (b) Sevenfold disclination, in blue, showing the Voronoi cell with seven nearest neighbors. (c) Burgers vector $\vec{b}$ and the corresponding dislocation shown by the green arrow.

The organization of this paper is as follows. In Sec. II, we describe the numerical method adopted in this investigation. Details of the algorithms are relegated to the Appendix. Our results for the zero-temperature distribution of defects for the two substrate morphologies considered are presented in Sec. III and compared to previous analytical theories, which we briefly review.

II. METHODS

A. System

Consider a system of N particles constrained to move on a two-dimensional (2D) surface embedded in a 3D space. The simulations were performed in a square simulation cell of area $A=b^2$, where b is the side length of the 2D projection of the surface onto the x-y plane. An embedded surface can be described in the Monge form $z=f(x,y)$ [25]. We investigate two different surfaces that are obtained from deforming a 2D flat plane. The first surface is created by two perpendicular intersecting sine waves, shown in Fig. 2(a).

The analytic representation is

$$f_s(x,y,b,a) = a\,\sin[x/b(2\pi)]\sin[y/b(2\pi)] \tag{2}$$

$$= a\,\sin(xq)\sin(yq), \tag{3}$$

where a is the amplitude of the sine wave and $q=\frac{2\pi}{b}$ the wave vector. The area element is given by

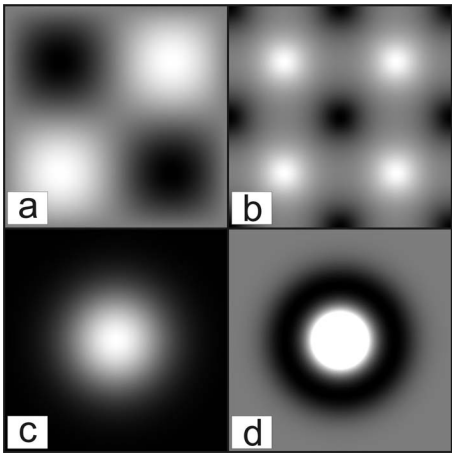

FIG. 2. (a) Contour plot of the height function of the sine-wave surface (f_s surface). (b) Gaussian curvature of the sine-wave surface shown in (a). (c) Corresponding plot for the isolated Gaussian bump (f_e surface) and its Gaussian curvature shown in (d).

$$d\sigma = \sqrt{1 + \left(\frac{\partial f_s}{\partial x}\right)^2 + \left(\frac{\partial f_s}{\partial y}\right)^2}\, dx\, dy \tag{4}$$

and the Gaussian curvature is

$$K = \frac{\frac{\partial^2 f_s}{\partial x^2}\frac{\partial^2 f_s}{\partial y^2} - \frac{\partial^2 f_s}{\partial x\, \partial y}^2}{\left[1 + \left(\frac{\partial f_s}{\partial x}\right)^2 + \left(\frac{\partial f_s}{\partial y}\right)^2\right]^2}. \tag{5}$$

A plot of the Gaussian curvature for this surface is shown in Fig. 2(b). The second surface is a Gaussian bump located at the center of the simulation cell. A height plot is shown in Fig. 2(c), adjacent to a plot of the Gaussian curvature for this surface shown in Fig. 2(d). The Monge representation of the surface reads

$$f_e(x,y,\sigma,a) = ae^{-(x^2+y^2)/2\sigma^2}, \tag{6}$$

where the standard deviation σ is equal to $\frac{1}{\sqrt{40}}$ for all simulations. This value was used to ensure a smooth height function at the boundary of the simulation box. The f_s and f_e surfaces show negative and positive Gaussian curvature, with a total Gaussian curvature ($\int_A K\, d\sigma = 0$) equal to zero. The f_e surface has azimuthal symmetry, and the region of negative curvature encloses a circle of positive curvature whose radius is determined from the position of the inflection point. The f_s surface, instead, displays a characteristic checkerboard pattern with the maximum absolute values of the negative and positive Gaussian curvature being equal.

The particles confined to the curved surface interact via an effective Yukawa pair potential $V(r)$. To a first approximation, a Yukawa potential describes the interaction between particles with surface charges dispersed in a solvent with counter-ions. In reduced units of $E^* = \frac{E}{Q^2/4\pi\epsilon_0}$, where Q is charge and ϵ_0 is the permittivity, it reads

TABLE I. Number of particles accommodating a hexagonal lattice for a square simulation cell.

Unit cells in the x direction	Unit cells in the y direction	Total number
26	15	780
19	11	418

$$V(r) = \frac{\exp(-\kappa r)}{r}[1/b_0], \tag{7}$$

where the constant κ is the inverse of the Debye-Hückel radius. The value for κ is kept constant at $100\frac{1}{b_0}$. The distance r between particles was calculated with Pythagoras's theorem in three dimensions, and not along the surface. This procedure has a closer resemblance to a diblock copolymer system or colloidal system in experiments. The added benefit is an increase in speed of the calculations due to the simpler expressions for r.

We start by laying down on a flat plane a hexagonal lattice of interacting particles. It is necessary to restrict the number of particles to integers so that the full hexagonal lattice can be accommodated in a square-shaped simulation cell. Table I shows the number of unit cells in the x and y directions where each unit cell contains two particles.

The density of the particles was kept constant for a given particle number. Since the deformation of the flat plane increases the surface area, the side length b was reduced to accommodate the change in total area, keeping the ratio (number of particles)/(area) constant. The total surface area of the surface is the integral over the simulation cell using the area element introduced in Eq. (4). The relation between the area and b is

$$(\text{area}) = \int_{-b/2}^{b/2}\int_{-b/2}^{b/2} d\sigma. \tag{8}$$

The area was chosen to be equal to 1, and b was changed accordingly.

B. Zero-temperature calculations

Elastic moduli of a Yukawa lattice

The elastic moduli of a lattice of particles interacting via a Yukawa potential can be directly derived from the pair potential itself. It has been shown by Medina-Noyola and Ivlev [26,27] that the Lamé constants μ and λ can be related to the Yukawa potential by using the two elements c_{11} and c_{66} from the elastic moduli matrix. Equations (9) and (10) describe the relation between the shear modulus $c_{66} = \mu$ and the compression modulus $c_{11} = \lambda + 2\mu$ and their relation to the pair-interaction potential V. The summations are taken over all crystal sites l, where V' denotes the first derivative and V'' the second derivative of the potential energy with respect to the interparticle distance r:

TABLE II. Elastic moduli of a Yukawa lattice for 418 and 780 particles.

N	$\mu(1/b_0^3)$	$\lambda(1/b_0^3)$	$Y(1/b_0^3)$
418	347	1137	1126
780	1911	8679	6476

$$c_{66} = \frac{N}{16}\sum_l [r_l^2 V''(r_l) + 3r_l V'(r_l)], \tag{9}$$

$$c_{11} = \frac{N}{16}\sum_l [3r_l^2 V''(r_l) + r_l V'(r_l)], \tag{10}$$

where N is the two-dimensional particle density and r_l is the distance to the neighbor at crystal site l. The values in Table II are approximate values that consider only interactions out to third nearest neighbors. In terms of Lamé constants, the Young's modulus reads [28]

$$Y = \frac{4\mu(\mu+\lambda)}{2\mu+\lambda}. \tag{11}$$

Table II shows a summary of the elastic coefficients for a Yukawa potential with $\kappa=100$ for the two different values of $N=418$ and $N=780$.

III. ZERO-TEMPERATURE DISTRIBUTION OF DEFECTS

In contrast to a sphere where an excess of 12 positive disclinations are present, no such constraints exist for the appearance of defects on a distorted plane due to the overall vanishing total Gaussian curvature. The vanishing total Gaussian curvature implies that in order to minimize the energy, two requirements must be satisfied. The sum over the coordination has to be conserved and equal to zero; this is a direct result of Eq. (1), $\Sigma_z(6-z)N_z=0$. Furthermore, the sum of all Burgers vectors arising from the dislocations has to be equal to zero for a crystal in the ground state. The ground state of a flat plane exhibits a defect-free hexagonal lattice, while even for a weakly distorted surface, the Gaussian curvature induces defects in the lattice to decrease the deformation energy. The deformation energy is described as the potential energy of the lattice on the distorted surface minus the potential energy of the defect-free hexagonal lattice on a flat plane.

Analytic work done in Ref. [19] predicts the critical aspect ratio $\xi_c=\frac{a}{\sigma}$ for the f_e surface, describing the point of transition from a defect-free to a defective lattice. A Gaussian bump with aspect ratio below ξ_c consists of a hexagonal lattice that wraps around the surface with considerable local distortion of the equilibrium bond distance while avoiding the creation of defects. Above ξ_c, a lattice with a finite number of defects becomes favorable over a defect-free lattice. The defects screen the Gaussian curvature from the rest of the lattice and, therefore, lower the deformation energy. The intuitive reason can be grasped by observing the behavior of parallel lines on surfaces of different curvature; see Fig. 3. In

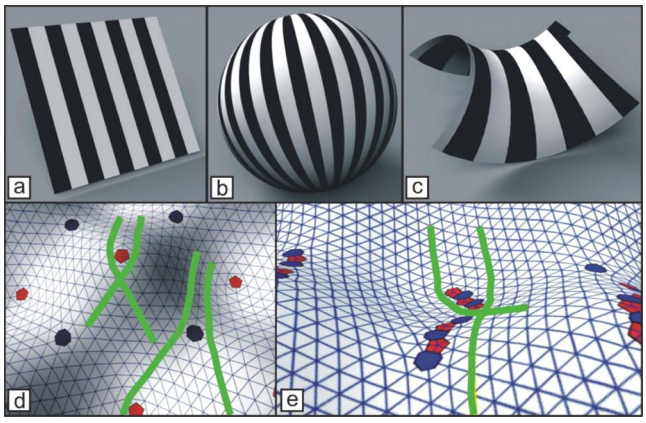

FIG. 3. (Color online) (a) Parallel lines on a flat plane. (b) Lines parallel on the equator merge on the poles of the positive Gaussian curvature surface. (c) Initially equidistant lines diverge on a saddle surface with negative Gaussian curvature. (d) Three-dimensional view of the triangulation of a lattice overlapped by the Voronoi cells of fivefold (red) and sevenfold (blue) disclinations. (e) Grain boundaries. The green lines are guides to the eye.

Fig. 3(a) parallel lines are plotted on a flat plane and by definition intersect at infinity. In the case of positive curvature, straight lines, which appear parallel along the equator of the sphere, do intersect at the poles. Negative Gaussian curvature will cause parallel lines to diverge as is shown in Fig. 3(c).

Curving a hexagonal lattice introduces strains that can be relieved by the introduction of defects at the price of some energy cost. The strain in the lattice caused by the geometric constraints associated with the curved substrate acts as a uniform external field that controls the equilibrium position of the dislocations. In Fig. 3(d), a three-dimensional view of a Delaunay triangulation [29] of a lattice on a curved surface is plotted. The blue polygons correspond to sevenfold disclinations and the red pentagons to fivefold disclinations. The yellow green lines are a guide to the eye, emphasizing the effect of disclinations on parallel lines in the lattice. The fivefold disclination focuses the green lines just as positive Gaussian curvature focuses parallel lines. The green lines on the right of Fig. 3(d) are caused to diverge due to the influence of the sevenfold disclination just as negative Gaussian curvature causes parallel lines to diverge. The effect of grain boundaries containing an uneven number of disclinations is similar to that of isolated disclinations and the inserted half rows can better relieve the frustration of weakly curved surfaces.

A. Gaussian bump surface

We will begin the investigation with a substrate shaped as an isolated Gaussian bump labeled the f_e surface, which is similar to the surface studied in Ref. [19] using 780 particles. A study with only 418 particles yielded similar results. A frustrated defect-free lattice embedded on a *gently* curved surface will exhibit a deformation energy increasing as a power law with the magnitude of the deformation. An ana-

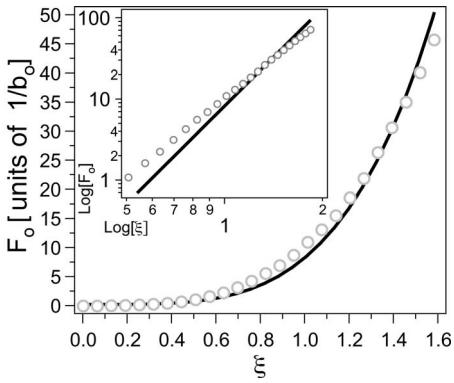

FIG. 4. Deformation energy F_0 (solid line) derived from the analytic expression in Eq. (12). Open circles (○) show the energy from deformation of hexagonal lattice calculated from Monte Carlo simulations. The inset shows the deformation energy in a log-log plot.

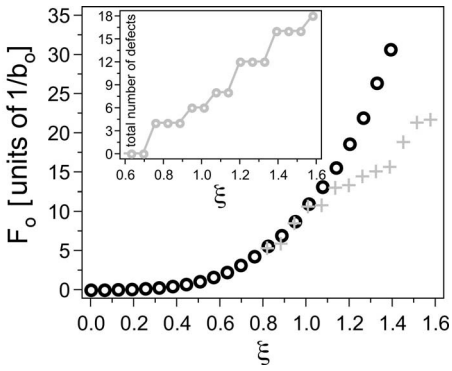

FIG. 5. Deformation energy of a lattice with 780 particles on a f_e surface. Open circles (○): F_0 for a defect-free lattice. Crosses (+): F_0 for a lattice that contains defects.

lytic expression derived within continuum elastic theory reads [30]

$$F_0 \cong \frac{Y\pi\sigma^2\xi^4}{64}, \tag{12}$$

where F_0 is the deformation energy, σ the variance of the Gaussian bump, and $\xi=\frac{a}{\sigma}$ the aspect ratio of the bump. Equation (12) is completely determined with no fitting parameters, and it is derived in the limit $\xi \ll 1$. A similar deformation energy can be extracted from the smart Monte Carlo (SMC) simulations discussed in the Appendix. The solid line in Fig. 4 shows the value of Eq. (12) as a function of ξ, while the open circles (○) are obtained from SMC simulations.

The value F_0 for the simulations is calculated by subtracting the potential energy of a relaxed hexagonal lattice in a flat plane from the potential energy of a defect-free hexagonal lattice wrapped on the surface of a given aspect ratio ξ. The defect density was monitored by determining the two-dimensional Voronoi diagram of particle positions in the x-y plane [31]. The Voronoi diagram was calculated in MATLAB using the QHULL sweep algorithms [29]. The isotropic initial state relaxed into a defect-free arrangement only up to a critical aspect ratio discussed below. Determining the value of F_0 for higher aspect ratios was achieved by seeding the simulations with an ordered initial condition. The seed was a hexagonal lattice in the x-y plane. The third dimension of each lattice point was added using Eq. (6). A SMC simulation was performed for 200 000 MC steps, while the temperature chosen suppressed the creation of defects, but still allowed movement of the particles. The SMC simulations were followed by a regular Metropolis algorithm at zero temperature for 200 000 MC cycles. It was possible to measure F_0 up to $\xi=1.6$. For values above $\xi>1.6$ the creation of defects could not be suppressed with the scheme described above. While there is qualitative agreement between the simulations and Eq. (12) in the regime $\xi \ll 1$ (for which its derivation holds), we observe systematic deviations as the deformation of the substrate measured by ξ becomes larger. The analytic value for F_0 increases as ξ^4, whereas the value calculated from simulations can be fit closely to a ξ^3 dependence. The inset of Fig. 4 shows the deformation energy in a log-log plot. We note that the continuum theory employed to derive Eq. (12) assumes that the scale on which the curvature changes is much larger than the lattice spacing, a regime that is not accessible to our simulations.

In Fig. 5 the deformation energy of a defect-free lattice is plotted [open circles (○)] versus the aspect ratio of the deformed surface f_e. The energy of a defective lattice is overlaid with crosses (+). In the region of low aspect ratio, a defect-free lattice yields the lowest deformation energy for the surface.

Three sources contribute to the energy of a lattice that contains defects: the potential energy of the lattice in flat space including the energy due to defects, the deformation energy from strain due to deformation of the lattice caused by the Gaussian curvature, and a third potential energy from the interaction between the Gaussian curvature and the defects. The deformation energy in the flat plane includes the elastic strain energy of individual defects, the core energies of these defects, and the defect interaction energy. The interaction energy between defects is also modified by the presence of a Gaussian curvature. For dislocations, this correction, which is proportional to the Burgers vector squared, is small in comparison to the direct interaction of each dislocation with the Gaussian curvature, which is linear in the Burgers vector $\vec{b}$. The interaction between Gaussian curvature and defects is generally a one-body potential energy of purely geometric origin that describes the coupling of an isolated defect to the Gaussian curvature.

An analytic form for the geometric potential of a dislocation is [30]

$$D(r,\theta) = -Y\alpha\sigma\frac{\xi^2}{8}\sin(\theta)\left[\left(\frac{1-e^{-r^2}}{r}\right)-\left(\frac{\sigma}{R}\right)^2 r\right], \tag{13}$$

where σ is the variance of the Gaussian bump and θ the angle between the Burgers vector of the dislocation and the gradient of the f_e surface. We have set the magnitude of the Burgers vector equal to the lattice spacing α. For angles θ (the angle is measured in clockwise direction) smaller than zero, the geometric potential becomes positive and the en-

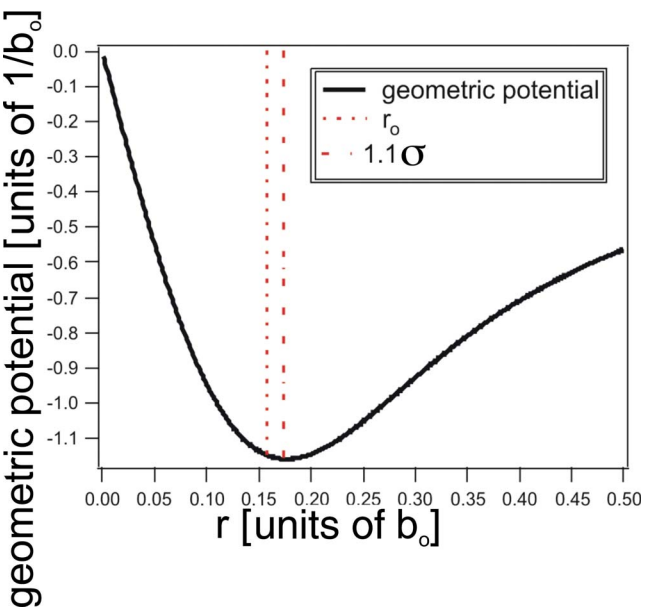

FIG. 6. (Color online) Geometric potential from Eq. (13) for $\theta=90°$.

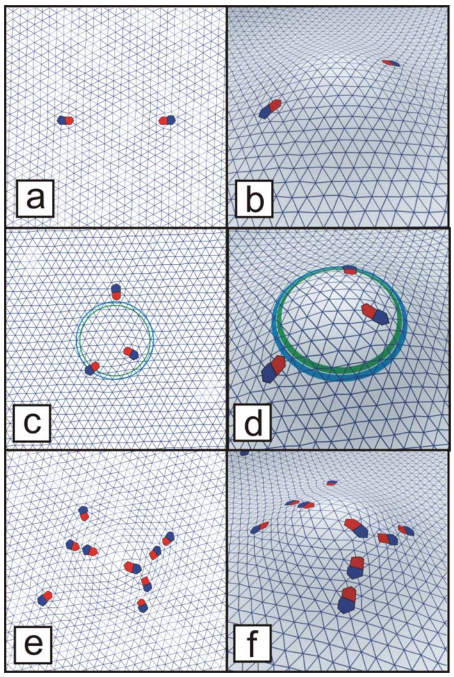

FIG. 7. (Color online) Delaunay triangulation of a 780-particle lattice on a curved f_e surface. (a) Top view of a lattice containing two defects with aspect ratio equal to 0.82. (b) Three-dimensional view of (a). (c) Three dislocations arranged around a Gaussian bump and the three-dimensional view in (d), the aspect ratio being equal to 0.95. (e) and (f) Top view and the corresponding three-dimensional view of a higher aspect ratio equal to 1.58.

ergy of the dislocation increases. For alignment of the Burgers vector parallel to the gradient ($\theta=0$), the geometric potential is equal to zero and the dislocation does not interact with the Gaussian curvature. The potential becomes attractive if the angle between the Burgers vector and the gradient is positive. This is the case if the fivefold disclination faces the area of positive curvature and the sevenfold disclination the opposite direction toward the area of negative Gaussian curvature. The second term in Eq. (13) $\left[\left(\frac{\sigma}{R}\right)^2 r\right]$ is a finite-size correction where R is the radius of the circular boundary of the system on which free boundary conditions are assumed. In the case of periodic boundary conditions, we estimate this term by setting $R=\frac{b}{2}$ where b is the size of the simulation square. The geometric potential is plotted for the f_e surface in Fig. 6 and exhibits a minimum at $r_0=1.1\sigma$, pulling the dislocations close to the inflection point of the Gaussian bump.

Above a critical aspect ratio of 0.76 for 780 particles on a f_e surface, isolated dislocations reduce the deformation energy of the lattice. The analytic value for the critical aspect ratio reads [30]

$$\xi_c^2 \approx c\frac{\alpha}{r_0}\ln\left(\frac{r_0}{b'}\right), \tag{14}$$

where $b'=\frac{\alpha}{2}e^{-8\pi E_c/Y\alpha^2}$, r_0 is the position of the minimum of the geometric potential, and $c\approx 1/2$. The equation yields a value of $\xi_c=0.49$ for a vanishing dislocation core energy $E_c=0$. A core energy of $1.15\frac{1}{b_0}$ for each of the two dislocations is required to match the value observed in the simulations. A reasonable estimate for the Yukawa lattice yields a value of $E_c\approx 0.1Y\alpha^2=0.96\frac{1}{b_0}$.

In Fig. 7, the arrangements of 780 particles on surfaces with three increasing aspect ratios are presented. In Fig. 7(a) two defects are observed. The center of the image coincides with the center of the Gaussian bump. They are rotated 180° with respect to each other, yielding a total Burgers vector of approximately zero. In Fig. 7(b) a three-dimensional side view is shown, illustrating how the defects arrange around the area of positive Gaussian curvature. The center of the dislocations is at 1.46σ with respect to the center of the bump and therefore farther away from the maximum Gaussian curvature than anticipated, but only by 1.5 lattice sites. The Burgers vectors of the dislocations make an angle of 90° with the gradient of the surface, minimizing the energy of the geometric potential.

In Figs. 7(c) and 7(d) the aspect ratio is 1.01. Three dislocations are observed, rotated 120° with respect to each other. The Burgers vectors are arranged clockwise around the center location of the Gaussian bump at an angle $\theta=90°$ with respect to the gradient of the f_e surface. A green circle marks the inflection point ($r=\sigma$) of the curvature, while the light blue circle highlights 1.1σ, the location of minimum geometric potential as calculated in Eq. (13). The good agreement between the angle θ and the theoretical prediction is due to the glide motion (parallel to the Burgers vector) of dislocations. During the cooling process of the Monte Carlo simulation, the defect can glide into the lowest-energy orientation with respect to the surface gradient without overcoming a large energy barrier.

Two of the three dislocations, however, are not in close proximity to the predicted distance from the top of the bump (1.1σ). One is deep inside the area of positive Gaussian curvature, while the other is in the region of negative Gaussian

curvature. In order to understand if the observed state is a trapped state due to the presumed high-energy barrier for the dislocation climb necessary to place the defects at the predicted position or represents a true equilibrium, three dislocations were placed at the positions predicted to yield the lowest energy. The distance between the dislocations was kept constant at seven lattice spacings. The 30 particles involved in the three dislocations were excluded from the displacement step during the Monte Carlo simulations. The Monte Carlo simulations resulted in a hexagonal lattice containing two additional dislocations besides the three dislocations placed around the top of the Gaussian bump. After removing the constraint on the 30 particles involved in the three dislocations, the number of total defects decreased to three dislocations arranged around the Gaussian bump with an angle of 120° with respect to each other. The distance r between the top of the bump and one of the dislocations was two lattice spacings larger than the predicted distance 1.1σ. Similar results were obtained after placing three dislocations around the bump with a distance between dislocations of six lattice spacings, thus placing the dislocations slightly closer to the top of the bump than predicted. It seems therefore that the deviation of the three dislocations from the position, 1.1σ, of lowest predicted energy from the continuum model corresponds to a minimum energy and does not result from kinetic trapping. It seems likely that the finite size of the system does not allow placement of three dislocations in close proximity to the predicted distance ($r=1.1\sigma$) from the top of the bump.

A lattice confined on a deformed surface f_e with aspect ratio equal to 1.58 is plotted in Fig. 7(e) and the three-dimensional view in Fig. 7(f). The arrangement and number of the dislocations for the high aspect ratio of 1.58 are governed by three factors. The total number of disclinations (a dislocation is made of two disclinations) is proportional to the aspect ratio and thus dependent on the amount of Gaussian curvature. The proportionality is shown in the inset of Fig. 5. The number of disclinations is an increasing function of the Gaussian curvature. A circular arrangement of dislocations as shown in Fig. 7(c) is energetically expensive for a large amount of dislocations. The more dislocations there are arranged in a ring around the center, the smaller the distance between individual dislocations with similar Burgers vectors becomes. The repulsive interaction between defects with similar Burgers vectors will increase the potential energy of the lattice. A transition to grain boundaries will occur when the repulsive interaction between dislocations at $\xi=1.10$ exceeds the decrease in energy due to placing the dislocations at the minimum of the geometric potential. The transition to grain boundaries is observed in the Monte Carlo simulations for more than four dislocations surrounding the Gaussian bump. In Figs. 7(e) and 7(f) nine dislocations are observed arranged in grain boundaries around the center of the Gaussian bump. The grain boundaries are not parallel to the gradient of the surface, but exhibit branching. The branching allows the dislocations to lower their potential energy. The closer each dislocation is to $1.1r_0$, the distance at which the geometric potential is a minimum, the lower their potential energy.

The dislocations and disclinations reduce the variance σ_{NN} of nearest-neighbor distances as illustrated in Fig. 8(a),

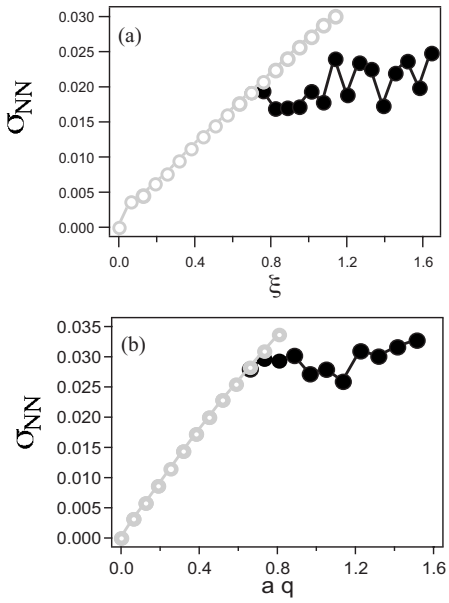

FIG. 8. (a) Variance σ_{NN} of the distribution of nearest-neighbor distances of a lattice confined on a f_e surface as a function of aspect ratio. (b) Variance σ_{NN} for a lattice on a f_s surface. Both graphs are for 780 particles. Open circles (○) are for a defect-free lattice and solid circles (●) for a defective lattice.

in agreement with the arguments of Travesset [13], that finding the ground state of particles is equivalent to finding the particle distribution that is closest to a perfect equilateral triangulation.

B. Sine-wave surface

We now turn to discuss the f_s surface which is generated by two sine waves intersecting perpendicularly to each other [see Eq. (2)]. As a result of the cubic symmetry of this substrate, the resulting defect configurations are more difficult to describe analytically than in the case of an isolated Gaussian bump. The discussion in the previous section can nonetheless provide a guide to understand the defect arrangements observed on the f_s surface. As a dimensionless parameter that describes the substrate deformation, we choose the product of the amplitude a times the magnitude of the wave vector, q, of the periodic surface (aq).

The ground state for a lattice on the f_s surface that has only a small deformation [i.e., below a critical value $(aq)_c$] is characterized by a defect-free hexagonal arrangement of particles. The critical value $(aq)_c$ will depend on the Young's modulus of the array, the core energy of the disclinations created, the defect interaction energy, and the deformation stress induced by the Gaussian curvature. Figures 9 and 10 show the deformation energy of a defect-free lattice and a defective lattice for 418 particles and 780 particles, respectively.

The deformation energy F_0 of the defect-free lattice was determined as described in the previous section and follows a power law with the same exponent equal to 3 as in the case of the f_e surface. Above a critical value $(aq)_c=0.8$, a lattice that contains defects has a lower deformation energy. Its en-

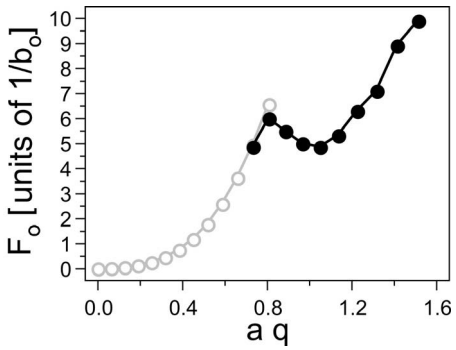

FIG. 9. Deformation energy of a lattice with 418 particles on a f_s surface. Open circles (○): F_0 for a defect-free lattice. Solid circles (●): F_0 for a defected lattice.

ergy, however, does not increase monotonically. The value of F_0 actually goes through a minimum around $aq=1.1$ for systems containing both 418 particles and 780 particles.

The absence of the radial symmetry of the deformation generates a directionality dependence of the geometrical potential $D(\vec{r},\theta)$ that depends on the position of $\vec{r}$, not just the radial distance from a chosen point (e.g., the f_e surface). The fivefold disclinations will be attracted by the regions of positive Gaussian curvature, and the sevenfold disclinations will be attracted by the regions of negative Gaussian curvature. The line of shortest distance between the area of maximum positive and negative curvature, L_s, minimizes the distance between the disclinations and their preferred Gaussian curvature and, therefore, minimizes the potential energy of the dislocation. The exact locus of the minimum dislocation potential energy lies exactly along the curve separating positive from negative Gaussian curvature on the surface, unlike the f_e surface discussed above where the point of lowest geometric potential is at 1.1σ. In the case of the f_s surface, the absolute value of the Gaussian curvature is symmetric across the zero-Gaussian-curvature boundary. A dislocation inside an area of positive Gaussian curvature is exposed to an attractive interaction between the fivefold disclination and the Gaussian curvature and a repulsive interaction of the sevenfold disclination with positive Gaussian curvature. The repulsion is stronger than the attraction pushing the dislocation out of the area of positive Gaussian curvature. The forces are

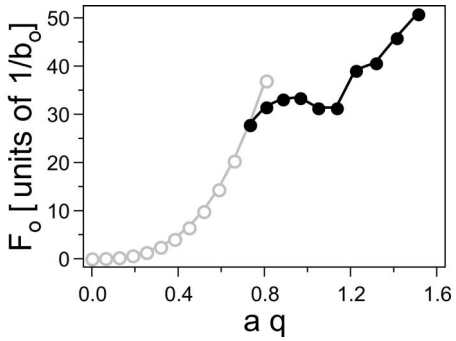

FIG. 10. Deformation energy of a lattice with 780 particles on a f_s surface. Open circles (○): F_0 for a defect-free lattice. Solid circles (●): F_0 for a defected lattice.

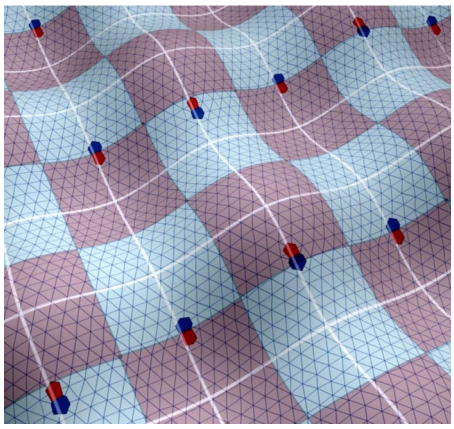

FIG. 11. (Color online) Three-dimensional view of a triangulation of a lattice with 418 particles on a f_s surface with $aq=0.81$. Dark red pentagons show the Voronoi cells of fivefold disclinations attached to dark blue sevenfold disclinations forming a dislocation. The white lines mark the shortest segments connecting the regions of maximum positive and maximum negative Gaussian curvature, L_s. The light red (blue) patches are areas of positive (negative) Gaussian curvature. The curvature is not constant inside the blue and red patches; see Fig. 2 for details.

equally strong in the negative Gaussian curved areas due to symmetry and, therefore, they center the dislocation between the area of positive and negative Gaussian curvature.

The positions of free dislocations for $aq=0.81$ in a lattice containing 418 particles are shown in a three-dimensional rendering in Fig. 11. The lattice is shown triangulated as black lines, overlaid with light-red and light-blue areas, corresponding to areas of positive and negative Gaussian curvature. The dislocations are highlighted with their Voronoi cells. The white lines mark the shortest line connecting the maximum positive and maximum negative Gaussian curvature, L_s. Red cells correspond to fivefold disclinations and blue cells to sevenfold disclinations. The dislocations align very close to the boundary between the positive and negative curved areas, the line of the zero Gaussian curvature. A top view of the configuration is shown in Fig. 12(a) and for 780 particles in Fig. 13(a).

Figure 11 shows that the exact position for some of the dislocations is not exactly on top of the zero-Gaussian-curvature line, but rather shifted along L_s, the line of shortest connection between maximum positive and negative Gaussian curvature. These configurations may not represent the equilibrated ground state. A lower-energy state from the current configuration can only be reached by a climb motion, which is energetically expensive.

An increase in aq leads to an increase in defects necessary to screen the stronger Gaussian curvature. In Figs. 12(c) and 12(d) the number of dislocations has doubled, going from $aq=0.81$ to $aq=0.89$. The dislocations cluster to form short grain boundary segments, as shown schematically in Fig. 14(a) rather than splitting up and screening the Gaussian curvature as in the case of the Gaussian bump. The short grain boundary [Fig. 14(a)] screens the Gaussian curvature better than the single dislocation [Fig. 14(b)]. Unlike the Gaussian bump where grain boundaries had to occur symmetrically to

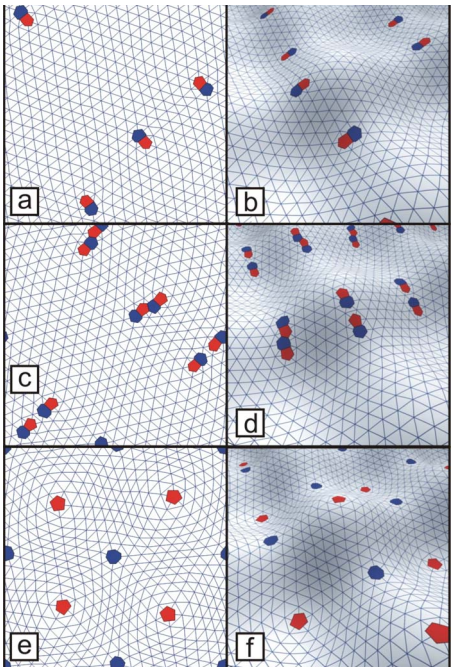

FIG. 12. (Color online) Delaunay triangulation of a 418-particle lattice on a curved f_s surface; fivefold disclinations are highlighted in red and sevenfold disclinations in blue. (a) Top view of a lattice containing four dislocations at $aq=0.81$. (b) Three-dimensional view of (a). (c) Eight dislocations symmetrically arranged along the zero-Gaussian-curvature line and (d) three-dimensional view of (c) at $aq=0.89$. (e) and (f) Top view and the corresponding three-dimensional view of free disclinations at $aq=1.13$.

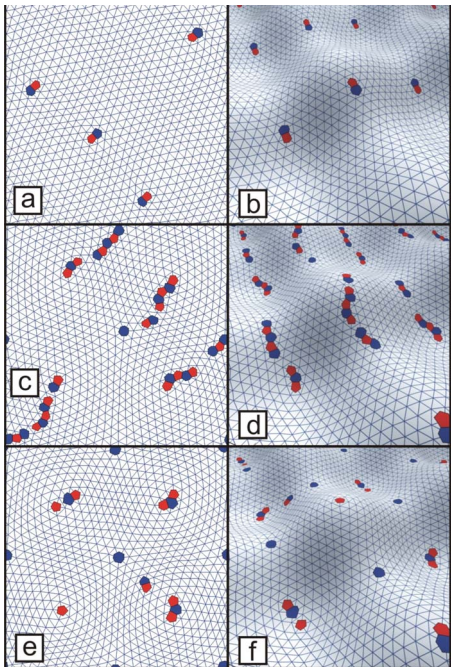

FIG. 13. (Color online) Delaunay triangulation of a 780-particle lattice on a curved f_s surface; fivefold disclinations are highlighted in red and sevenfold disclinations in blue. (a) Top view of a lattice containing four dislocations at $aq=0.81$. (b) Three-dimensional view of (a). (c) Eight dislocations symmetrically arranged along the zero-Gaussian-curvature line and (d) three-dimensional view of (c) at $aq=0.97$; (e) and (f) Top view and the corresponding three-dimensional view of free disclinations at $aq=1.32$.

surround the point of maximum curvature, the symmetry of the f_s surface forces the dislocations to occupy the same side of the simulation cell in order to ensure that the total Burgers vector vanishes. However, there are two degenerate orientations of this dislocation array: one as shown in Fig. 11 and the second that is obtained from the first by a 90° rotation. An alternative arrangement with grain boundaries rotated 90° with respect to each other was also observed, but yielded higher deformation energy.

The low density lattice with 418 particles shows a very narrow range of aq where dislocations or short grain boundaries are stable, above which an arrangement of disclinations at the location of maximum Gaussian curvature yields the minimum energy. The critical value of aq for this transition from dislocations to free disclinations is at $aq>0.89$. There are no dislocations present for values above the critical value for 418 particles. A top view is shown in Fig. 12(e) and the three-dimensional view in Fig. 12(f) for $aq=1.08$. The value of 0.89 coincides with the onset of a decrease in deformation energy (see Fig. 9). It is apparent from the continuing decrease in deformation energy as free disclinations are formed that the free disclinations better accommodate the higher Gaussian curvature. Seung and Nelson [32] examined a two-dimensional surface embedded in three-dimensional space containing a single positive or negative disclination and showed that buckling reduces the energy of the disclination compared to flat space. In reverse, a lattice forced to conform to a curved surface reduces its deformation energy by introducing a disclination. The minimum at $(aq)=1.02$ may therefore resemble the closest match between the f_s surface and an unconstrained surface buckling under the stress induced by a single disclination.

A similar transition from free dislocations to free disclinations is seen for the surface with 780 particles, but it does not occur as abruptly with increasing Gaussian curvature as it does for the 418-particle case. Grain boundaries extend along the entire length of the segment L_s, connecting the areas of maximum positive and negative curvature. Each grain boundary is terminated with a disclination of matching preference, fivefold for positive and sevenfold for negative Gaussian curvature. The transition to free disclinations for the case of 780 particles occurs by the separation of disclinations or a disclination attached to a dislocation from the ends of the grain boundary, see Fig. 13(c) as a top view and Fig. 13(d) as a three-dimensional view. The grain boundaries screen the strain induced in the lattice by the disclinations. The difference between the 418- and 780-particle samples is consistent with previous studies of crystallography on spheres of increasing radius. For small radius, the topological constraint of Eq. (1) on the total number of disclinations is satisfied by placing 12 isolated disclinations at the vertices of an icosahedron (inscribed in the sphere). As the radius is increased, grain boundaries arise in the ground state to reduce the deformation energy of the lattice [5,6,10,13].

In Fig. 15 the total number of defects is plotted as solid circles (●) and the total number of free disclinations with

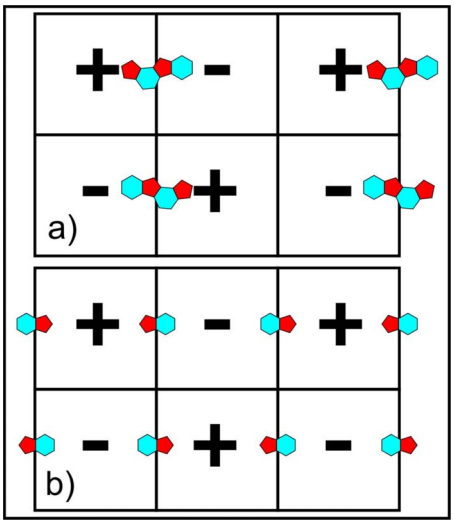

FIG. 14. (Color online) Two possible defect configurations that satisfy the requirement of zero net Burgers vector. Configuration (a) characterized by short grain boundaries is favored energetically over the arrangement of isolated dislocations shown in configuration (b).

open circles (○) for 780 particles on a f_s surface. The total number of free disclinations shows a slow increase for 780 particles, while the total number of disclinations for 418 particles shows a sharp steplike function, presented in Fig. 16. Figures 13(e) and 13(f) show a structure equivalent to the free disclination arrangement seen in Figs. 12(e) and 12(f), just with grain boundary scars still present. The scars in Figs. 13(e) and 13(f) are concentrated around the fivefold disclinations, corroborating a trend seen in Figs. 13(c) and 13(d). At $aq=1.32$ free sevenfold disclinations are present, while the fivefold defects are still attached to a dislocation, forming a small scar. All of the sevenfold disclinations in Figs. 13(e) and 13(f) are free disclinations, whereas only one out of four fivefold disclinations is isolated. This is somehow surprising, since the Gaussian curvature for negative and positive disclinations is equal in absolute value. Seung and Nelson calculated the deformation energy, and unlike in flat space where positive and negative disclinations have the same energy, the negative disclination exhibits higher deformation energy than the positive disclination. It is not clear if the small scars around the fivefold disclinations are a trapped state or result from the interplay between the fivefold disclinations and the Gaussian curvature. As in the case of the isolated bump, the dislocations and disclinations reduced the variance of nearest-neighbor distances shown in Fig. 8(b).

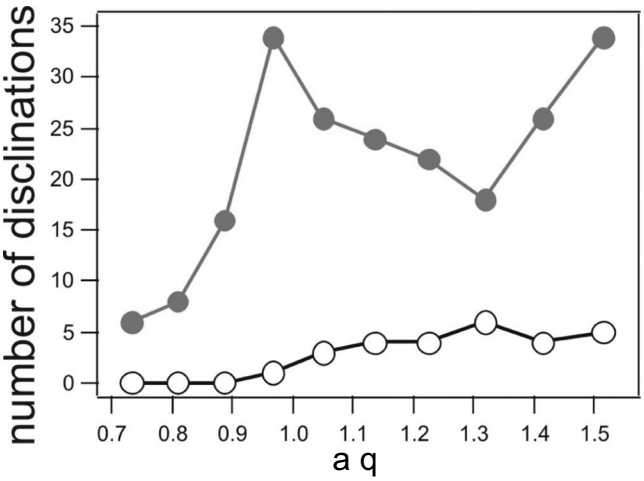

FIG. 15. Solid circles (●): n, the total number of disclinations. Open circles (○): n_f, the number of free disclinations for 780 particles.

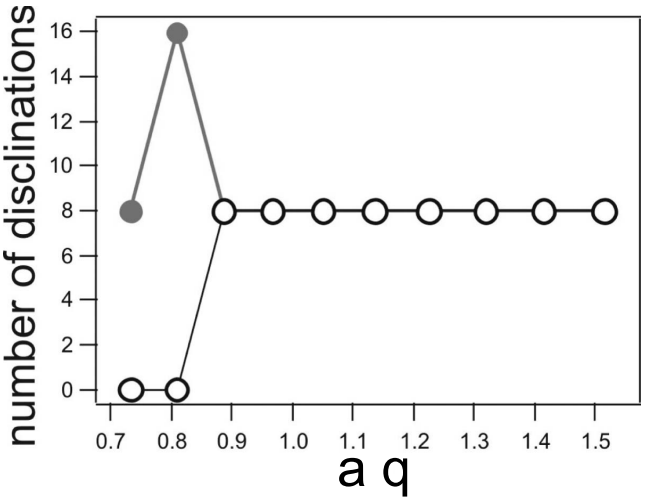

FIG. 16. Solid circles (●): n, the total number of disclinations. Open circles (○): n_f, the number of free disclinations for 418 particles. The number of dislocations is equal to $(n-n_f)/2$ since a dislocation is a bound pair of a fivefold and a sevenfold disclination.

IV. CONCLUSION

We developed a Monte Carlo algorithm to study ground states of Yukawa particles on weakly curved surfaces. The scheme is easily adopted to different potentials as well as different surface deformations. We find good agreement with analytical predictions of deformation energy and defect positions made in Ref. [19]. A critical aspect ratio is observed, above which the incorporation of defects in the lattice lowers the deformation energy as well as the width of the distribution of nearest-neighbor distances. A surface shaped as a Gaussian bump shows a wide variety of arrangements for dislocations as the aspect ratio is increased as well as an increase in the numbers of the dislocations. The orientation of single defects is governed by the Gaussian curvature, such that the Burgers vectors of the dislocations are parallel to the circle of zero Gaussian curvature. The radial distance of the dislocations away from the center of the bump is close to the circle of zero Gaussian curvature, matching closely the minima of the geometric potential located at 1.1ξ, calculated in Ref. [19]. We did not observe isolated disclinations on the f_e surface for the aspect ratios investigated. A defect-free lattice was also observed below a critical value of $(aq)_c$ for particles confined on a surface described by two perpendicularly intersecting sine waves. The dislocations align along

the shortest line L_s connecting the maximum positive and maximum negative Gaussian curvature. The symmetry between the positive and negative Gaussian curvature positions the dislocations at the line of zero Gaussian curvature. Grain boundary scars grow along L_s with increasing aq, until they connect the areas of maximum positive and negative Gaussian curvature. Since no further growth of grain boundary scars is possible to screen the Gaussian curvature, the ground state evolves to produce free disclinations. The disclinations in the case of the larger particle numbers are attached to grain boundary scars, thus reducing the strain in the lattice due to the disclinations, in a similar way to the grain boundary scars observed on surfaces of large spheres.

ACKNOWLEDGMENTS

This work was supported by the NSF Polymer Program under Grant No. DMR0704539 and benefited from use of the Central Facilities of the UCSB Materials Research Laboratory, which is supported by the MRSEC Program of the NSF under Grant No. DMR05-20415. V.V. and G.H.F. acknowledge financial support from NSF Grants Nos. DMR05-47230 and DMR06-03710, respectively. We thank David Nelson, Randall Kamien, and Tom Lubensky for useful discussions.

APPENDIX: SMART MONTE CARLO SCHEME

The results presented in this paper were calculated using a "smart Monte Carlo" scheme devised by Rossky, Doll, and Friedman [33,34]. The trial displacement of a particle i from position m to position n can be written as

$$\delta\mathbf{r}_i^{nm} = \beta A\mathbf{f}_i^m + \delta\mathbf{r}_i^G, \tag{A1}$$

where A is an adjustable parameter to control the acceptance rate of the trial move, $\beta=\frac{1}{T^*}$, where T^* is in units of k_BT (k_B is the Boltzmann's constant and T the absolute temperature in kelvin), $\mathbf{f}_i^m$ is the force acting on particle i at position m, and $\delta\mathbf{r}_i^G$ is a random displacement whose components are chosen from a Gaussian distribution, with zero mean and variance $\langle(\delta r_{ix}^G)^2\rangle=\langle(\delta r_{iy}^G)^2\rangle=2A$, which was computed using a polar form of the Box-Muller transformation [35]. A trial displacement $\delta\mathbf{r}_i^{xyG}$ is performed in the x-y plane, while the actual displacement vector $\delta\mathbf{r}_i^G$ lies in the local tangent plane of the particle i [36,37]. We therefore corrected the trial move $\delta\mathbf{r}_i^{xyG}$ as shown in Eq. (A5) for the x direction and Eq. (A6) for the y direction of the f_e surface. The expressions $\delta\mathbf{r}_{ix}^{xyG}$ and $\mathbf{r}_{iy}^{xyG}$ are the components of the trial move in the x and y directions of the flat plane. For the f_e surface the correction factor $u(x,y)$ is shown in Eq. (A3) and the correction factor $v(x,y)$ in Eq. (A4):

$$f_e(x,y) = a\,\exp\left(-\frac{(x^2+y^2)}{2\sigma^2}\right), \tag{A2}$$

$$u(x,y) = \frac{1}{\sqrt{1+\left(\frac{f(x,y)}{\sigma^2}x\right)^2}}, \tag{A3}$$

$$v(x,y) = \frac{1}{\sqrt{1+\left(\frac{f(x,y)}{\sigma^2}y\right)^2}} \tag{A4}$$

$$\Rightarrow(\delta r_{ix}^{xyG})_c = \delta r_{ix}^{xyG}u(x,y), \tag{A5}$$

$$(\delta r_{iy}^{xyG})_c = \delta r_{iy}^{xyG}v(x,y). \tag{A6}$$

A similar calculation for the f_s surface is presented in Eqs. (A7)–(A9) below:

$$f_s(x,y) = a\,\sin(xq)\sin(yq), \tag{A7}$$

$$u(x,y) = \frac{1}{\sqrt{1+a^2q^2\,\cos(xq)\sin(yq)}}, \tag{A8}$$

$$v(x,y) = \frac{1}{\sqrt{1+a^2q^2\,\sin(xq)\cos(yq)}}. \tag{A9}$$

The force $\mathbf{f}_i^m$ acting on a particle i at position m on the curved surface is calculated in three dimensions and projected straight down onto the x-y plane for the trial displacement contribution. The force was calculated from the Yukawa potential

$$\mathbf{f} = -\nabla[V(x,y,z)], \tag{A10}$$

and for the force between particle i and particle j we obtain

$$\mathbf{f}_{ij} = \frac{V(r)}{r^2}(1+\kappa r)\mathbf{r}, \tag{A11}$$

where $r=\sqrt{x^2+y^2+z^2}$ and $\mathbf{r}=x\hat{e}_x+y\hat{e}_y+z\hat{e}_z$ are the distance and vector, respectively, in three dimensions between particle i and a neighboring particle j. The total force acting on particle i, $\mathbf{f}_i^m$, is the sum over the particles labeled by j that are neighbors to particle i, $\Sigma_j\mathbf{f}_{ij}$. The trial displacement in the x-y plane then can be written as follows:

$$\delta\mathbf{r}_{ixy}^{nm} = \beta A(f_{ix}^m, f_{iy}^m, 0) + (\delta r_{ix}^{xyG})_c\hat{e}_x + (\delta r_{iy}^{xyG})_c\hat{e}_y, \tag{A12}$$

where $\delta\mathbf{r}_{ixy}^{nm}$ is the two-dimensional trial displacement in the flat x-y plane and f_{ix}^m the x component of the total force acting on particle i. The particle move is accepted with the probability $\min(1, \alpha_{nm}\rho_n/\alpha_{mn}\rho_m)$, where the ratio is [34]

$$\frac{\alpha_{nm}\rho_n}{\alpha_{mn}\rho_m} = \exp\left[-\beta\left(\delta V_{nm} + \frac{1}{2}(\mathbf{f}_i^n+\mathbf{f}_i^m)\cdot\delta\mathbf{r}_i^{nm} + \delta W^{SMC}\right)\right], \tag{A13}$$

α_{nm} is the stochastic matrix going from state m to state n with equal probability, ρ_n/ρ_m is the acceptance probability, and

$$\delta W^{SMC} = \frac{\beta A}{4}[(\delta \mathbf{f}_i^{nm})^2 + 2\mathbf{f}_i^m \cdot \delta \mathbf{f}_i^{nm}]. \tag{A14}$$

For the zero-temperature study, the initial condition was a hexagonal lattice. The system was then annealed at sufficiently high temperature T^* to completely melt the system. The following cooling process into the crystalline phase was taken over 1×10^6 Monte Carlo steps. To retrieve the potential energy, the system was sampled for an additional 70 000 MC steps at zero temperature using a regular Metropolis algorithm [38] to avoid divergences in the trial displacements. This procedure was repeated at least 40 times, and the lowest-energy configuration was then analyzed.

[1] J. J. Thomson, Philos. Mag. **7**, 237 (1904).
[2] B. K. Ganser, S. Li, V. Y. Klishko, J. T. Finch, and W. I. Sundquist, Science **283**, 80 (1999).
[3] J. Heuser, J. Cell Biol. **108**, 401 (1989).
[4] T. Kohyama, D. M. Kroll, and G. Gompper, Phys. Rev. E **68**, 061905 (2003).
[5] A. R. Bausch, M. J. Bowick, A. Cacciuto, A. D. Dinsmore, M. F. Hsu, D. R. Nelson, M. G. Nikolaides, A. Travesset, and D. A. Weitz, Science **299**, 1716 (2003).
[6] T. Einert, P. Lipowsky, J. Schilling, M. J. Bowick, and A. R. Bausch, Langmuir **21**, 12076 (2005).
[7] P. Leiderer, Z. Phys. B: Condens. Matter **98**, 303 (1995).
[8] W. Z. Helfrich, Z. Naturforsch. [C] **28**, 693 (1973).
[9] A. E. Lobkovsky and T. A. Witten, Phys. Rev. E **55**, 1577 (1997).
[10] M. J. Bowick, D. R. Nelson, and A. Travesset, Phys. Rev. B **62**, 8738 (2000).
[11] A. Travesset, Phys. Rev. B **68**, 115421 (2003).
[12] S. Schneider and G. Gompper, Europhys. Lett. **70**, 136 (2005).
[13] A. Travesset, Phys. Rev. E **72**, 036110 (2005).
[14] M. J. Bowick, A. Cacciuto, D. R. Nelson, and A. Travesset, Phys. Rev. Lett. **89**, 185502 (2002).
[15] M. J. Bowick, A. Cacciuto, D. R. Nelson, and A. Travesset, Phys. Rev. B **73**, 024115 (2006).
[16] D. R. Nelson, Phys. Rev. Lett. **50**, 982 (1983).
[17] J. P. Gaspard, R. Mosseri, and J. F. Sadoc (unpublished).
[18] S. Sachdev and D. R. Nelson, J. Phys. C **17**, 5473 (1984).
[19] V. Vitelli, J. B. Lucks, and D. R. Nelson, Proc. Natl. Acad. Sci. U.S.A. **103**, 12323 (2006).
[20] L. Giomi and M. J. Bowick, Phys. Rev. B **76**, 054106 (2007).
[21] A. Hexemer, Ph.D. thesis, UC Santa Barbara, 2006.
[22] V. Vitelli and A. M. Turner, Phys. Rev. Lett. **93**, 215301 (2004).
[23] V. Vitelli and D. R. Nelson, Phys. Rev. E **70**, 051105 (2004).
[24] P. M. Chaiken and T. C. Lubensky, *Principles of Condensed Matter Physics* (Cambridge University Press, Cambridge, England, 2000).
[25] E. W. Weisstein, http://mathworld.wolfram.com/MongePatch.html
[26] M. Medina-Noyola and B. I. Ivlev, Phys. Rev. E **52**, 6281 (1995).
[27] E. H. Brandt, J. Low Temp. Phys. **26**, 735 (1977).
[28] L. D. Landau and E. M. Lifschitz, *Theory of Elasticity* (Butterworth-Heinemann, Oxford, 1995).
[29] C. B. Barber, D. P. Dobkin, and H. T. Huhdanpaa, ACM Trans. Math. Softw. **22**, 469 (1996).
[30] V. Vitelli, Ph.D. thesis, Harvard University, 2006.
[31] G. F. Voronoi, J. Reine Angew. Math. **136**, 67 (1909).
[32] H. S. Seung and D. R. Nelson, Phys. Rev. A **38**, 1005 (1988).
[33] P. J. Rossky, J. D. Doll, and H. L. Friedman, J. Chem. Phys. **69**, 4628 (1978).
[34] M. P. Allen and D. J. Tildesley, *Computer Simulations of Liquids* (Oxford Science, Oxford, 1999).
[35] G. E. P. Box and M. E. Muller, Ann. Math. Stat. **29**, 610 (1958).
[36] R. Holyst, D. Plewczynski, A. Aksimentiev, and K. Burdzy, Phys. Rev. E **60**, 302 (1999).
[37] T. C. Petersen, I. K. Snook, I. Yarovsky, and D. G. McCulloch, Phys. Rev. B **72**, 125417 (2005).
[38] N. Metropolis, A. W. Rosenbluth, M. N. Rosenbluth, A. H. Teller, and E. Teller, J. Chem. Phys. **21**, 1087 (1953).